# Vacuum polarization effects in baryon-loaded magnetar bursts and implications for x-ray polarization

Tomoki Wada*

*Frontier Research Institute for Interdisciplinary Sciences, Tohoku University, Sendai, Japan; Astronomical Institute, Graduate School of Science, Tohoku University, Sendai, Japan and Department of Physics, National Chung Hsing University, Taichung, Taiwan*

(Received 2 September 2025; revised 5 November 2025; accepted 7 November 2025; published 15 December 2025)

Magnetars provide natural laboratories for strong-field quantum electrodynamics processes, such as vacuum polarization, which gives rise to vacuum resonance together with the plasma response. We develop a general framework to describe vacuum resonance in a three-component plasma consisting of ions, electrons, and positrons, as expected in baryon-loaded magnetar bursts. By introducing a parametrization of the plasma composition, we establish the general criterion for the occurrence of vacuum resonance in such plasmas. Our analysis encompasses both Mikheyev-Smirnov-Wolfenstein-like adiabatic mode conversion and nonadiabatic eigenmode transition, highlighting their dependence on the plasma composition. Applying this framework to baryon-loaded fireballs in magnetar bursts, we estimate the characteristic x-ray polarization signatures. Detection of these polarizations will provide observational signatures of vacuum polarization as well as baryon loading in magnetar fireballs.

DOI: 10.1103/k3hz-k6v4

## I. INTRODUCTION

Magnetars are neutron stars with magnetic fields that may exceed the critical quantum electrodynamic (QED) field strength of $B_Q = m_e^2 c^3/(e\hbar) = 4.4 \times 10^{13}$ G, where $m_e$ is the electron mass, $c$ is the speed of light, $e$ is the elementary charge, and $\hbar$ is the reduced Planck constant. Their persistent surface x-ray emission and bursting activity are interpreted as being powered by the intense magnetic fields [1–5]. A sudden release of magnetic energy near a magnetar surface can trigger the formation of a fireball, a plasma, consisting mainly of electron-positron pairs, strongly coupled with photons [6,7]. These fireballs are capable of being the source of bursting x-ray emission from magnetars. Bursts are classified according to their total luminosity: $\lesssim 10^{44}$ erg s$^{-1}$ for short bursts (SBs), and $\gtrsim 10^{44}$ erg s$^{-1}$ for giant flares (GFs) [4]. In addition to x-ray bursts, magnetars have been proposed as sources of fast radio bursts (FRBs), MeV gamma rays, cosmic rays, or ultrahigh-energy neutrinos [e.g., [8–11] ]. Owing to their strong magnetic field, magnetars serve as natural laboratories for phenomena under strong magnetic fields [12], such as photon splitting [13], single-photon pair production, and vacuum birefringence due to vacuum polarization [14], through their observations.

In strong magnetic fields, vacuum polarization predicted by nonlinear QED theory [15,16] modifies photon propagation [17–19], particularly near the vacuum resonance, at which its influences become comparable to those of the plasma [20–23]. In the magnetar environment, both strong magnetic fields and plasmas are present [24]. While each contribution alone alters x-ray propagation, their combination can also significantly affect photon propagation through so-called vacuum resonance. The vacuum resonance arises when the contributions from strong magnetic fields and plasmas become comparable. This phenomenon has been extensively studied in the context of magnetar atmospheric emission [23,25–34], where an electron-ion plasma is assumed to exist near the magnetar surface. The vacuum resonance is also known to occur in relativistically streaming electron-positron plasmas [35]. In these previous works, the plasma was assumed to be either an electron-ion plasma or an electron–positron plasma, that is, to be a two-component plasma.

Recently, X-ray polarization measurements with the Imaging X-ray Polarimetry Explorer (IXPE) [36] have opened a new window for probing magnetospheric and surface emission processes in magnetars. Energy-dependent x-ray polarization of magnetar persistent surface emission has been observed in some magnetars [37–42]. Remarkably, one of them, 4U 0142 + 6, exhibits about a 90-degree swing in the polarization angle in low energy and high energy [37], a feature expected from vacuum

*Contact author: tomoki.wada@astr.tohoku.ac.jp

*Published by the American Physical Society under the terms of the Creative Commons Attribution 4.0 International license. Further distribution of this work must maintain attribution to the author(s) and the published article's title, journal citation, and DOI.*

resonance [43], although resonant Compton scattering in a twisted magnetosphere can also produce such swings [44,45]. These x-ray polarization measurements of magnetars indicate that x-ray polarization from magnetars may serve as direct evidence of strong-field physics, beyond the critical QED field $B_Q$. Although polarization during the magnetar burst phase remains unexplored, it might be detected in the future by IXPE or planned eXTP [46].

In magnetar bursts, their super-Eddington x-ray luminosity can drive baryon-loaded fireballs, thereby introducing ion contributions to the dielectric properties of the plasma. In most SBs, the fireball is confined by large-scale closed magnetic field lines, since its thermal energy density is much smaller than the magnetic energy density. At the footpoints of the trapped fireball, strong radiation pressure can ablate baryons from the magnetar surface and load them into the fireball [6,47]. In contrast, during GFs, the thermal energy density of the fireball can exceed the magnetic field energy density, allowing it to expand with little magnetic confinement, similar to fireball models for gamma-ray bursts [48,49]. In this case, baryons can be loaded into the fireball, enhancing the kinetic energy of the associated plasma outflow [50–52], as suggested in the observation of the GF from SGR 1806-20 [53–56] and its radio afterglow [57–59]. In some of SBs, fireballs can expand along magnetic field lines if it forms near the magnetic pole [60]. The Galactic FRB associated with an SB from the Galactic magnetar, SGR 1935 + 2154 [61–66] may originate from such a polar fireball [67–73]. The large kinetic energy of a baryon-loaded fireball offers a favorable energy budget for this Galactic FRB [73]. These theoretical expectations and observations both indicate the presence of baryons in the fireballs in magnetar bursts; quantifying the baryon content is fundamental for understanding these bursting activities.

In this work, we derive the general condition for vacuum resonance in such baryon-loaded fireballs, and evaluate its effect on the emergent x-ray polarization. The baryon loading in fireballs introduces a vacuum resonance, which is well studied in magnetar persistent surface emission [23,25–32], but not previously considered in detail for magnetar bursts. This resonance occurs when the plasma and vacuum polarization contributions to the dielectric tensor are comparable, enabling x-ray photons to convert between polarization eigenmodes and thereby modifying the observed polarization.

This paper is organized as follows. We introduce our model in Sec. II A. Section II B presents an analysis of the photon normal modes. In Sec. III, we investigate the propagation modes of photons over the vacuum resonance, Mikheyev-Smirnov-Wolfenstein (MSW)-like conversion (Sec. III A) and nonadiabatic mode transition (Sec. III B). The observational expectations of these results are presented in Sec. IV. Section V is devoted to the summary and discussion. For simplicity, we do not consider the detailed baryonic composition and treat all baryons as protons in this study.

## II. NORMAL MODES OF ELECTROMAGNETIC WAVES IN BARYON-LOADED FIREBALLS

We first describe the formation of a three-component (electron-positron-baryon) plasma, and photon propagation in it, including the effect of vacuum polarization. The scenarios for baryon loading in magnetar bursts and the setup of our model are described in Sec. II A. We examine the normal modes of electromagnetic waves in Sec. II B.

### A. Baryon-loading onto fireballs in magnetar bursts

We first describe the physical setup of our study: baryon-loaded fireballs in magnetar bursts. A sudden release of magnetic energy near the magnetar surface triggers the formation of a fireball. Initially, the plasma may consist solely of electron-positron pairs created via pair creation. However, baryons on the magnetar surface are ablated by the photons and entrained into its plasma because the luminosity exceeds the Eddington limit [6,47]. Consequently, a baryon-loaded fireball naturally forms in a magnetar burst, and its plasma is described as a three-component plasma.

The composition of the three-component plasma depends on the geometry and location of the fireball (Fig. 1). In a trapped fireball, the baryonic component would be distributed so as to maintain hydrostatic equilibrium between the radiation pressure and the magnetar's gravity, leading to a higher baryon contribution to the particle number density at the base of the closed magnetic field lines [6]. In an expanding fireball, the baryon contribution becomes dominant in the outer region, where the pair number density decreases relative to the inner regions due to pair annihilation. In both cases, baryon loading naturally occurs, and a strongly magnetized

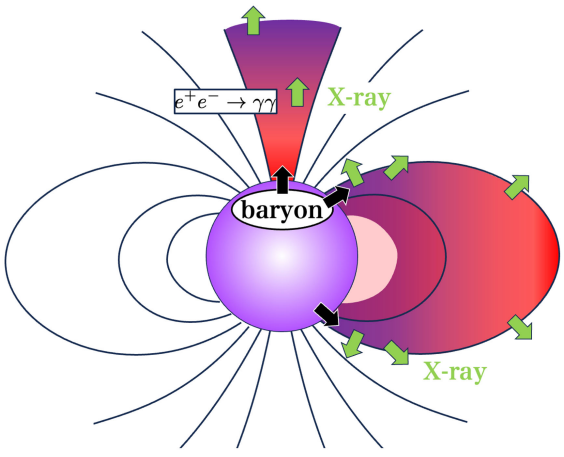



FIG. 1. Schematic picture of baryon-loaded fireballs in magnetar bursts; a trapped fireball (right) and an expanding fireball (top). The coexistence of the two fireballs is not required.

three-component plasma, consisting of baryons, positrons, and electrons, is realized (see Sec. IV A for more details).

In order to characterize this three-component plasma, we define the relevant variables. The number densities of electrons, positrons, and baryons are denoted by $n_-$, $n_+$, and $n_b$, respectively. They satisfy the charge-neutrality condition

$$n_- = n_+ + n_b. \tag{1}$$

We introduce a parameter $f$ to quantify the baryon content of the plasma,

$$f = \frac{n_b}{n_-}, \tag{2}$$

such that the limit of $f \to 1$ corresponds to an electron-ion plasma, while $f \to 0$ corresponds to a purely electron-positron pair plasma. The plasma frequency for each component is defined as

$$\omega_{ps} = \sqrt{\frac{4\pi n_s e^2}{m_s}}, \tag{3}$$

where $B$ is the strength of a magnetic field and $s = -, +, b$, and $m_s$ is the mass of species $s$. The corresponding cyclotron frequency is

$$\omega_{Bs} = \frac{eB}{m_s c}. \tag{4}$$

These frequencies satisfy the closure relation

$$\omega_{p-} = (1-f)^{-1/2}\omega_{p+} = (f\mu)^{-1/2}\omega_{pb} \tag{5}$$

$$\omega_{B-} = \omega_{B+} = \mu^{-1}\omega_{Bb} \tag{6}$$

where $\mu = m_e/m_p \ll 1$.

### B. Normal modes of electromagnetic waves with vacuum polarization in a three-component plasma

Dielectric tensor and inverse permeability tensor consist of contributions from the standard plasma component and from the vacuum polarization. Throughout this paper, the plasma is treated within the cold plasma approximation, whereby its thermal velocity is neglected. In a coordinate system with the $z$-axis aligned with the magnetic field, the dielectric tensor takes the form [e.g., [12,23] ]

$$\boldsymbol{\varepsilon} = \begin{pmatrix} \epsilon & ig & 0 \\ -ig & \epsilon & 0 \\ 0 & 0 & \eta \end{pmatrix} + \begin{pmatrix} A_V - 1 & 0 & 0 \\ 0 & A_V - 1 & 0 \\ 0 & 0 & A_V - 1 + Q_V \end{pmatrix}, \tag{7}$$

where the first term on the right-hand side corresponds to the plasma contribution of the three-component plasma, and the second term corresponds to the vacuum contribution. The quantities $\epsilon$, $g$, $\eta$ are given by [e.g., [12] ]

$$\epsilon = 1 + \frac{(2-f)v}{u-1} + \frac{f\mu v}{\mu^2 u - 1}, \tag{8}$$

$$g = -\frac{fvu^{1/2}}{u-1} + \frac{\mu^2 fvu^{1/2}}{\mu^2 u - 1}, \tag{9}$$

$$\eta = 1 - v(2 - f + \mu f), \tag{10}$$

where $u = \omega_{B-}^2/\omega^2$, and $v = \omega_{p-}^2/\omega^2$. Throughout this paper, we use the notation $u_s = \omega_{Bs}^2/\omega^2$ and $v_s = \omega_{ps}^2/\omega^2$ for $s = +, b$. The vacuum terms are [e.g., [27] ]

$$A_V \simeq \begin{cases} 1 - 2\delta_V & (b \ll 1) \\ 1 + \frac{\alpha}{2\pi}\left[1.2 - \frac{2}{3}\ln b - \frac{1}{b}(0.86 + \ln b) - \frac{1}{2b^2}\right] & (b \gg 1) \end{cases}, \tag{11}$$

$$Q_V \simeq \begin{cases} 7\delta_V & (b \ll 1) \\ -\frac{\alpha}{2\pi}\left[-\frac{2}{3}b + 1.3 - \frac{1}{b}(0.31 + \ln b) - \frac{0.70}{2b^2}\right] & (b \gg 1) \end{cases}, \tag{12}$$

where $\delta_V = \alpha b^2/(45\pi)$, $\alpha$ is the fine-structure constant, and $b = B/B_Q$. The inverse permeability tensor is [e.g., [27] ]

$$\boldsymbol{\mu} = \begin{pmatrix} 1 & 0 & 0 \\ 0 & 1 & 0 \\ 0 & 0 & 1 \end{pmatrix} + \begin{pmatrix} A_V - 1 & 0 & 0 \\ 0 & A_V - 1 & 0 \\ 0 & 0 & A_V - 1 + M_V \end{pmatrix}, \tag{13}$$

where [e.g., [27] ]

$$M_V = \begin{cases} -4\delta_V & (b \ll 1) \\ -\frac{\alpha}{2\pi}\left[\frac{2}{3} + \frac{1}{b}(0.15 - \ln b) - \frac{1}{b^2}\right] & (b \gg 1) \end{cases}. \tag{14}$$

In the weak-field limit, $b \to 0$, the vacuum terms satisfy $A_V - 1 \to 0$, $Q_V \to 0$, $M_V \to 0$. In this paper, we focus on waves with frequencies much larger than the plasma frequency, that is, $v \ll 1$. In the limit $f \to 0$, Eqs. (7)–(10) reproduce to the dielectric tensor of pair plasma [e.g., [74] ], and in the limit $f \to 1$ and for $\mu \ll 1$, they reduce to the dielectric tensor of an electron-ion plasma including vacuum contribution [e.g., [3,27] ]. For simplicity, as in [23], we neglect the wave damping, which would introduce an imaginary contribution into the dielectric tensor [12,22].

The normal modes of propagating waves can be explicitly obtained as follows. For an electromagnetic wave $\vec{E}$ with frequency $\omega$ propagating along a newly defined $z$-axis,

the propagation is governed by the wave equation [e.g., [12,23] ],

$$-k_\pm^2 \vec{e}_z \times [\boldsymbol{\mu} \cdot (\vec{e}_z \times \vec{E}_\pm)] = \frac{\omega^2}{c^2} \boldsymbol{\varepsilon} \cdot \vec{E}_\pm, \tag{15}$$

where $k_\pm$ is the wave vector and $\vec{e}_i$ $(i = x, y, z)$ is a unit vector in the direction of $i$. The subscripts "±" label the two eigenmodes for the quantities associated with the wave. Here, starting from the previous coordinate system, where the tensor components are given by Eqs. (7)–(10) and wave vector is set to be on the $x$-$z$ plane, we perform a rotation in the $x$-$z$ plane such that the wave vector is aligned with the $z$-axis. The unit eigenvector $\vec{E}_\pm$ can be expressed explicitly in this rotated coordinate system, using the angle $\theta_{kB}$ between the magnetic field and the wave vector. We decompose $\vec{E}_\pm$ as $\vec{E}_\pm = (\vec{E}_{\pm,\mathrm{T}} + E_{\pm,z}\vec{e}_z)/(1 + {E_{\pm,z}}^2)^{1/2}$, where $\vec{E}_{\pm,\mathrm{T}}$ is a normalized transverse component. The transverse component is

$$\vec{E}_{\pm,\mathrm{T}} = \frac{1}{(1 + K_\pm^2)^{1/2}} (iK_\pm \vec{e}_x + \vec{e}_y), \tag{16}$$

where these vectors are unit and mutually orthogonal. By substituting these expressions and the rotated forms of Eqs. (7) and (13) (rotated by $\theta_{kB}$ in the $x$-$z$ plane) into Eq. (15) and eliminating $E_{\pm,z}$, we obtain the eigenmodes of electromagnetic waves. For the eigenmodes, $K_\pm$ equals

$$K_\pm = \beta \pm \sqrt{\beta^2 + R_V}, \tag{17}$$

where

$$\beta = \frac{(-\epsilon_\mathrm{v}^2 + \epsilon_\mathrm{v}\eta_\mathrm{v}(1 + M_V/A_V) + g_\mathrm{v}^2)\sin^2\theta_{kB}}{2 g_\mathrm{v}\eta_\mathrm{v}\cos\theta_{kB}}, \tag{18}$$

$\epsilon_\mathrm{v} = \epsilon + A_V - 1$, $\eta_\mathrm{v} = \eta + A_V - 1 + Q_V$, $g_\mathrm{v} = g$, and $R_V = 1 + (M_V/A_V)\sin^2\theta_{kB} \simeq 1$. [75] The refractive indices of these eigenmode, $N_\pm = ck_\pm/\omega$, satisfy [e.g., [12] ]

$$N_\pm^2 = \frac{R_V\epsilon_\mathrm{v}\eta_\mathrm{v} + \epsilon_\mathrm{v}^2\sin^2\theta_{kB} + \epsilon_\mathrm{v}\eta_\mathrm{v}\cos^2\theta_{kB} - g_\mathrm{v}^2\sin^2\theta_{kB} \pm 2\eta_\mathrm{v} g_\mathrm{v}\cos\theta_{kB}\sqrt{\beta^2 + R_V}}{2A_V R_V(\epsilon_\mathrm{v}\sin^2\theta_{kB} + \eta_\mathrm{v}\cos^2\theta_{kB})}. \tag{19}$$

Substituting Eqs. (8)–(10) into Eq. (18) and using $A_V - 1$, $Q_V, M_V, \mu \ll 1$ give the explicit formula for $\beta$ in terms of wave frequencies as

$$\beta = \frac{u^{1/2}(1 - u_b)\sin^2\theta_{kB}}{2\cos\theta_{kB}} \left(\frac{2 - f}{f}\right) \left[1 - \frac{(M_V + Q_V)(1 - u^{-1})}{v(2 - f)}\right]. \tag{20}$$

The factor of $(2 - f)/f$ explicitly represents the effect of the three-component plasma. Here, the divergence of $|\beta|$ as $f \to 0$ implies that the transverse components cannot be normalized according to Eq. (16): one of $x$ or $y$ components becomes zero. As an example, for $\beta > 0$, at the limit of $f \to 0$ (i.e., $\beta \to \infty$), one finds $K_+ \to \infty$ and $K_- \to 0$ [Eq. (17)], and hence $\vec{E}_+ \| \vec{e}_x$ and $\vec{E}_- \| \vec{e}_y$ [Eq. (16)]. This limit corresponds to the pair-plasma limit in which the eigenmodes of the wave separate into the O-mode, whose electric field lies in the $x$–$z$ plane, and the X-mode, whose electric field is perpendicular to that plane. The factor $v(2 - f) = v + v_+$ in the right-hand term represents the plasma frequency for the electron-positron pair component. If an electromagnetic wave propagates adiabatically, i.e., remains in its eigenmode, the transverse components of the electric field are given by Eqs. (16), (17), and (20).

The propagation eigenmodes are elliptically polarized and can be represented as the + and − modes, distinguished by the handedness of their polarization [see Eq. (17)]. In contrast, the electron response to the wave is primarily determined by the angle between the transverse component of the background magnetic field and the wave's electric field. In this term, the modes are classified into X-mode ($\vec{E} = \vec{e}_y$ in the basis of Eq. (16)) and O-mode ($\vec{E} = \vec{e}_x$), both of which are eigenmodes in purely pair plasma. Since the propagation eigenmodes do not coincide with the X/O-modes, photons can undergo conversion between the X- and O-modes during adiabatic propagation.

## III. ADIABATIC AND NONADIABATIC MODE TRANSFORMATIONS

When photons propagate in a three-component plasma, both adiabatic mode conversion and nonadiabatic mode transition can occur. In Sec. III A, we consider the adiabatic limit, in which a photon remains in the +/− eigenmode, leading to conversion between X- and O-modes at the vacuum resonance. This phenomenon is formally analogous to the MSW oscillation in neutrino physics. In Sec. III B, we investigate nonadiabatic transitions between + and − eigenmodes in the vicinity of the vacuum resonance.

### A. Adiabatic Mikheyev-Smirnov-Wolfenstein mode conversion around the vacuum resonance

The vacuum resonance is defined as $\beta = 0$ [23], that is, the transverse electric fields are circularly polarized, $\vec{E}_{\pm,\mathrm{T}} \simeq (\pm i\vec{e}_x + \vec{e}_y)/\sqrt{2}$ [see Eq. (16)]. This condition is satisfied due to the comparable contribution from the vacuum polarization and the plasma at [see Eq. (20)],

$$(2-f)v_{\mathrm{res}} = (M_V + Q_V)(1-u^{-1}). \tag{21}$$

For a given magnetic field, Eq. (21) contains two independent variables, frequency $\omega$ and electron-positron number density $n_e = n_+ + n_- = (2-f)n_-$. For a fixed electron-positron number density, the condition in Eq. (21) gives the vacuum resonance frequency. Conversely, for a photon with frequency $\omega$, this condition can be expressed in terms of the total pair number density as

$$n_{e,\mathrm{res}} = \frac{m_e\omega^2}{4\pi e^2}(M_V + Q_V)(1-u^{-1}). \tag{22}$$

The wave propagating from an inner, high-density region to an outer, low-density region encounters the vacuum resonance when Eq. (22) is satisfied. Around this density, MSW-like conversion occurs. Stochastic nonadiabatic transitions between eigenmodes will be discussed in Sec. III B. In the three-component plasma, the condition for vacuum resonance is determined solely by the total pair-particle number density, unlike the case of the magnetar surface emission where the condition is determined by the electron number density [19,23].

Figure 2 shows the normalized $K_\pm$ for different values of $f$. The horizontal axis gives the electron-positron number density in unit of $\sigma n_e$, where $\sigma = \sigma_{\mathrm{T}} \times \min(1, u^{-1})$ [76,77], $\sigma_{\mathrm{T}}$ is the Thomson cross section, and cyclotron resonance is ignored for this normalization. The adopted parameters are $B = 10^{13}$ G, $\theta_{kB} = \pi/4$, and $\hbar\omega = 10$ keV. The solid lines correspond to normalized $K_+$, and dashed lines represent normalized $K_-$. As the wave propagates from a high-density region to a low-density region, the direction of the $+$ mode electric field rotates from the $x$ direction to the $y$ direction [see Eq. (16)], corresponding to a transition from an O-mode to an X-mode. In contrast, the $-$ mode rotates from the $y$ direction to the $x$ direction, that is, from an X-mode to an O-mode. As shown in Eq. (20), as $\beta$ decreases from a value $\beta \gg 1$, crosses zero, and continues decreasing to $\beta \ll -1$, the quantity $K_+$ ($K_-$) evolves from a large positive value, $2|\beta|$ [a small negative value, $-1/(2|\beta|)$], through 1, and to a small positive value, $1/(2|\beta|)$ (a large negative value, $-2|\beta|$). The X/O-modes are conversed in this way. This process is analogous to the MSW mechanism for neutrino oscillation: the photon remains in its $\pm$ eigenmode, and the X/O-modes are adiabatically converted.

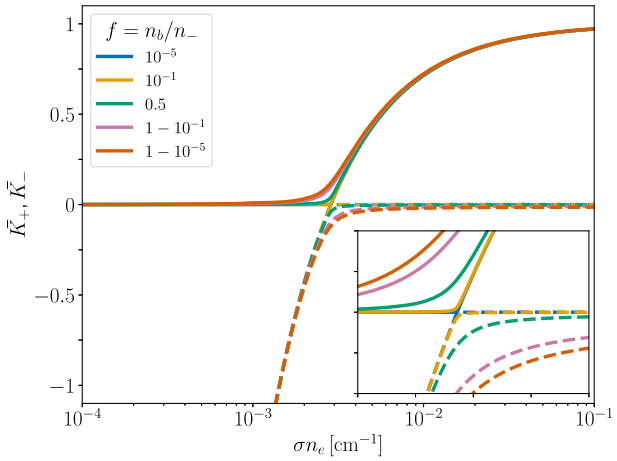



FIG. 2. Electron-positron density dependence of $\bar{K}_\pm$, defined as $K_\pm$ normalized by the maximum value of $K_+$ in the large $\sigma n_e$ limit. Solid lines correspond to $K_+$, and dashed lines to $K_-$. Different colors indicate different values of $f$ [see Eq. (2)]. The curves for $f = 10^{-5}, 10^{-1}, 0.5, 1-10^{-1}$, and $1-10^{-5}$ are further normalized by a factor of $1.6\times10^6$, $1.6\times10^2$, $2.5\times10^1$, $1.0\times10$, and 8.3, respectively. The inset shows curves around the vacuum resonance in a linear scale.

The behavior of $K_\pm$ varies with $f$. For smaller $f$ values (nearly pair plasma), both elliptically polarized modes retain their handedness but approach linear polarization: the polarization ellipses become highly flattened, with the electric field predominantly along the $x$ or $y$ axes. In addition to the ellipticity, the gap between the $+$ and the $-$ modes is smaller than that of larger $f$ values. This difference affects the probability of nonadiabatic mode transitions at the vacuum resonance, which will be discussed in Sec. III B.

### B. Nonadiabatic mode transition around the vacuum resonance

A photon propagating from a high-density region to a low-density region (from right to left in Fig. 2) can nonadiabatically transition from one eigenmode to the other. In such transition, a photon in $\pm$ mode stochastically jumps to $\mp$ mode, that is, from the solid (dashed) line to the dashed (solid) line in Fig. 2. Thus, X(O)-mode in the high-density region remains X(O)-mode in the low-density region across the vacuum resonance. The conditions and probabilities for such nonadiabatic mode transitions are analyzed in this subsection.

To quantify the adiabatic propagation and nonadiabatic mode transition, we compute the corresponding probabilities in a three-component plasma following the procedure of [23]. Rewriting $\vec{E}_{\pm,\mathrm{T}}$ in Eq. (16) as,

$$\vec{E}_{+,\mathrm{T}} = i\cos\theta_m\vec{e}_x + \sin\theta_m\vec{e}_y, \tag{23}$$

$$\vec{E}_{-,\mathrm{T}} = -i\sin\theta_m\vec{e}_x + \cos\theta_m\vec{e}_y, \tag{24}$$

a general polarized electromagnetic wave with frequency $\omega$ can be expanded by these basis vectors as,

$$\vec{E}_{\rm T} = A_+(z)e^{i\phi_+}\vec{E}_{+,\rm T} + A_-(z)e^{i\phi_-}\vec{E}_{-,\rm T}, \tag{25}$$

where $\phi_\pm = \int^z k_\pm dz$ and $A_\pm(z)$ is the amplitude function. The mixing angle $\theta_m$ satisfies

$$\tan 2\theta_m = \beta^{-1}. \tag{26}$$

We adopt the WKB approximation, in which $A_\pm$ and $\vec{E}_{\pm,\rm T}$ vary on a scale much longer than the wavelength. Under this approximation, $k_\pm \gg |A'_\pm(z)/A_\pm(z)|, |E^{j\prime}_{\pm,T}/E^j_{\pm,\rm T}|$ ($j = x$, $y$ and $E^j_{\pm,\rm T}$ are the components of vector $\vec{E}_{\pm,\rm T}$), where a prime denotes $d/dz$. Substituting Eq. (25) into the wave equation [Eq. (15)], and applying the WKB approximation yields the following equation for $A_\pm$ [23],

$$i\frac{d}{dz}\begin{pmatrix}\mathcal{A}_+\\ \mathcal{A}_-\end{pmatrix} \simeq \begin{pmatrix}-\frac{\Delta k}{2} & i\theta'_m\\ -i\theta'_m & \frac{\Delta k}{2}\end{pmatrix}\begin{pmatrix}\mathcal{A}_+\\ \mathcal{A}_-\end{pmatrix}. \tag{27}$$

Here, $\mathcal{A}_\pm = A_\pm(z)e^{i\phi_\pm}$, $\Delta k = k_+ - k_-$, and we have used $|\Delta k/k_\pm| \ll 1$, which follows from $v \ll 1$ and $g \ll \epsilon, \eta$ [see Eqs. (8)–(10)]. A nonessential unity matrix has been subtracted. As in [23], the modes evolve almost adiabatically if $|\Delta k/(2\theta'_m)| \gg 1$ is satisfied. However, for

$$\gamma = \left|\frac{\Delta k}{2\theta'_m}\right| \ll 1, \tag{28}$$

which is easily satisfied for $\Delta k \sim 0$ (see Eq. (29) later), the nonadiabatic transition becomes significant. This nonadiabatic conversion is a so-called Landau-Zener transition [78,79].

The probability for a nonadiabatic mode transition is determined by the adiabaticity parameter $\gamma$ at the vacuum resonance. Using $\epsilon_{\rm v}, \eta_{\rm v} \gg g_{\rm v}$, which follows from $v \ll 1$, together with Eqs. (8)–(10), (19), and (26), we obtain the difference between the refractive indices for $+$ and $-$ modes as

$$N_+ - N_- = -\frac{u^{1/2}}{u-1}\frac{fv}{1-u_b}\frac{\cos\theta_{kB}}{\sin 2\theta_m}. \tag{29}$$

From Eqs. (26), (28), and (29), $\gamma$ can be expressed in terms of the relevant frequencies as

$$\gamma = \frac{2\omega}{c}\frac{f^2}{\tan^2\theta_{kB}\sin^3 2\theta_m} \times \frac{v^3}{uv'(1-u_b)^2(1-u^{-1})^2(M_V+Q_V)}. \tag{30}$$

The probability of a nonadiabatic transition from one eigenmode to the other is then given by the Landau-Zener formula [e.g., [80,81]]:

$$P_{\rm NA} = \exp\left(-\frac{\pi}{2}\gamma_{\rm res}\right), \tag{31}$$

where $\gamma_{\rm res}$ is the value of $\gamma$ evaluated at $v_{\rm res}$ [see Eq. (21)],

$$\gamma_{\rm res} = \frac{2\omega}{c}\frac{1}{\tan^2\theta_{kB}}\left(\frac{f}{2-f}\right)^2\frac{M_V+Q_V}{(1-u_b)^2}\frac{H_{\rm res}}{u}, \tag{32}$$

where $H_{\rm res} = v_{\rm res}/v'_{\rm res}$. $\gamma_{\rm res}$ can be rewritten as $\gamma_{\rm res} = (2/\pi)(\omega/\omega_{\rm adi})^3$, [82] where

$$\frac{\hbar\omega_{\rm adi}}{m_e c^2} = \left[\frac{\hbar}{\pi m_e c}\frac{\tan^2\theta_{kB}(1-u_b)^2}{H_{\rm res}(M_V+Q_V)}\left(\frac{B}{B_Q}\right)^2\left(\frac{2-f}{f}\right)^2\right]^{1/3}. \tag{33}$$

The nonadiabatic transition becomes significant for photons with $\omega < \omega_{\rm adi}$ The specific values of $\omega_{\rm adi}$ will be examined in Sec. IV.

The implications of nonadiabatic transitions in the extreme limits of $f$ are as follows. In the limit $f \to 1$, the result reproduces that for the electron-ion plasma, as studied in the context of persistent surface emission [23,27]. In this case, the nonadiabatic transition probability depends explicitly on the photon energy. For intermediate $f$ values, as may occur in baryon-loaded fireballs in magnetar bursts, both of the adiabatic photon propagation and nonadiabatic mode transition can occur, resulting in mode changes from X(O)-mode to O(X)-mode or preserving its X(O)-mode (see Sec. IV). In the opposite limit $f \to 0$ (purely pair plasma), $\gamma_{\rm res}$ converges to 0 [Eq. (32)], yielding

$$\lim_{f\to 0} P_{\rm NA} = 1. \tag{34}$$

Thus, an X(O)-mode photon retains its X(O)-mode, rather than its eigenmode, across the vacuum resonance. In this limit, MSW-like conversions do not occur, and the X- and O-eigenmode description in a pair plasma, where vacuum resonance is not expected, is recovered due to nonadiabatic mode transitions.

## IV. OBSERVATIONAL IMPLICATION OF VACUUM RESONANCE IN MAGNETAR BURSTS

Using the results in Sec. III and analytic models of baryon-loaded fireballs, we investigate the impacts of the vacuum resonance on the polarization properties of magnetar bursts. In Sec. IVA, we show, from timescale considerations, that the thermal equilibrium plasma is realized in magnetar bursts. The polarization of x-ray emission from a trapped fireball is examined in

Sec. IV B, while that from an expanding fireball is considered in Sec. IV C. The primary aim of this section is to demonstrate, within a simplified analytic framework, how vacuum resonance investigated in the previous sections influences the x-ray polarization from magnetar bursts. While detailed and global calculations are important, they are beyond the scope of this work. The essential physics can be captured with the approach adopted here. Throughout this section, we set $\hbar = 1$.

### A. Three-component plasma in magnetar bursts

In magnetar bursts, which are intrinsically time-dependent phenomena, the fireball itself can exhibit variability. Fireballs are thought to form through the dissipation of magnetohydrodynamic waves in the magnetosphere [6]. A sudden displacement of the magnetar crust excites Alfvén waves. For a crustal displacement of $\Delta\ell$, the characteristic frequency is estimated as $\sim V_\mu/\Delta\ell \sim 10^4\ \mathrm{s}^{-1}\Delta\ell_{,4}^{-1}\rho_{,11}^{1/6}$, where $\mu = 2\times10^{27}\ \mathrm{erg\,cm^{-3}}\rho_{,11}^{4/3}$ is the shear modulus of the crust [83], $\rho$ is the crustal density, $V_\mu = (\mu/\rho)^{1/2}$ is the sound speed in the crust, and the notation $Q_{,x} = Q/10^x$ denotes normalization in cgs units. The shear modulus is evaluated assuming that the crust is isotropic body-centered cubic polycrystal with atomic number 40 and mass number 120 [83]. $\Delta\ell \sim 10^4$ cm is comparable to the hydrostatic pressure scale height of the outer crust. The fireball variability timescale is given by the inverse of this frequency, $t_{\rm var} \sim 10^{-4}\ \mathrm{s}\Delta\ell_{,4}\rho_{,11}^{-1/6}$. The injected Alfvén waves dissipate through magnetospheric instability on the magnetospheric Alfvén crossing timescale, $t_{\rm diss} \sim r_{\rm fb}/c \sim 3\times10^{-5}\ \mathrm{s}\, r_{\rm fb,6}$, where $r_{\rm fb}$ is the characteristic fireball radius and Alfvén speed is assumed to be $c$. An optically thick electron-positron pair fireball thus forms on this timescale, possibly modulated on $t_{\rm var}$. Baryons are subsequently loaded from the magnetar surface with this variable timescale.

In trapped fireballs, the three-component plasma remains in hydrostatic and local thermal equilibrium. The hydrostatic equilibrium is established on a timescale of $t_{\rm hyd} \sim r_{\rm fb}/(c/\sqrt{3}) \sim 2\times10^{-5}\ \mathrm{s}\, r_{\rm fb,6}$, where $c/\sqrt{3}$ is the sound speed in a radiation-dominated fluid. After baryons and their associated electrons are loaded into the pair fireball, the positrons will annihilate with these electrons. Near the photospheric radius, the pair-annihilation timescale is $t_{\rm ann} \sim 8/(3\sigma_T c n_-) \sim 1\times10^{-7}\ \mathrm{s}\, T_{,10\ \mathrm{keV}}^2 B_{,14}^{-2} r_{\rm fb,6}$, where $T_{,10\ \mathrm{keV}} = T/(10\ \mathrm{keV})$ is the temperature of the plasma. Here, we have adopted the nonrelativistic limit in which the product of cross section for pair annihilation and relative velocity is $3\sigma_{\rm T}c/8$. For simplicity, we consider the photospheric radius where the optical depth for pair plasma is unity, i.e., $2n_-\sigma(T,B)r_{\rm fb} \sim 1$, where $\sigma(T,B) = (4\pi^2/5)(T/(m_e c^2))^2(B/B_Q)^{-2}\sigma_{\rm T}$ is the Rosseland mean of the scattering cross section [6,12]. Because $t_{\rm ann} \ll t_{\rm hyd} < t_{\rm var}$, both hydrostatic and local thermal equilibrium would be maintained within the trapped fireball.

In the simplest case of expanding fireballs, the three-component plasma remains in local thermal equilibrium, but hydrostatic equilibrium cannot be maintained due to its expansion at relativistic speeds. For expanding fireball, times and densities are evaluated in the plasma comoving frame. The dynamical timescale is $t_{\rm dyn} \sim r/(c\Gamma) \sim 1\times10^{-5}\ \mathrm{s}\, r_{,6}\Gamma_{,0.4}$, where $r$ is the radial distance from the magnetar center and $\Gamma$ is the bulk Lorentz factor. The pair-annihilation timescale is $t_{\rm ann} \sim 8/(3\sigma_{\rm T}cn_-) \sim 3\times10^{-8}\ \mathrm{s}\, T_{,10\ \mathrm{keV}}^2 B_{,14}^{-2} r_{\rm fb,6}\Gamma_{,0.4}^{-1}$, where we have assumed $2n_-\sigma(T,B)r/\Gamma \sim 1$. The variability timescale in the comoving frame is $t_{\rm var} \sim 3\times10^{-5}\ \mathrm{s}\Delta\ell_{,4}\rho_{,11}^{-1/6}\Gamma_{0.4}^{-1}$. Consequently, the condition $t_{\rm ann} \ll t_{\rm dyn}, t_{\rm var}$ is satisfied, and local thermal equilibrium is achieved.

For fireballs expanding within a narrow magnetic flux tube, the timescale of photon diffusion perpendicular to the flux tube can be shorter than the dynamical timescale. In such cases, the fireball may evolve into a two-component structure: a baryon-loaded fireball confined to the initial flux tube and a surrounding pair-plasma fireball formed by the diffused photons [73]. In addition, temporal variations in the x-ray luminosity may lead to corresponding changes in the baryon fraction. However, we do not consider these details in this work. Instead, we focus on cases where the baryon content is taken to be uniform in both space and time, so that the effects of vacuum polarization can be clearly demonstrated.

### B. Polarization of trapped fireballs

The x-ray spectrum from trapped fireballs has been modeled in [84], showing good agreement with observations. In a magnetized plasma, the scattering cross section for X-mode photons is suppressed by a factor of $\sim(\omega/\omega_{B-})^2 = u^{-1}$ for $\omega < \omega_{B-}$, resulting in a spectrum almost composed of X-mode photons [84]. Consequently, lower-energy x-ray photons escape from the inner region of the fireball with a higher temperature, producing a spectrum flatter than a blackbody. [84] demonstrated that the emergent x-ray spectrum can be characterized by a single parameter, the brightness temperature $T_b$.

In the context of the vacuum resonance, the relative location of the photospheric radius and the vacuum resonance determines the resulting polarization [23]. In a fireball with a given $T_b$, photons of energy $\omega$ escape from the depth where the temperature is [84]

$$T_\omega = T_b\sqrt{1+\frac{3\pi^2}{5}\left(\frac{T_b}{\omega}\right)^2}. \tag{35}$$

At the location, the baryon number density should be around the value obtained from the hydrostatic equilibrium condition [6], and is parametrized by $\mathcal{F}_{\rm trap}$ as

$$n_{b,\mathrm{trap}} = -\frac{\mathcal{F}_{\mathrm{trap}}}{m_b g_{\mathrm{NS}}}\frac{d}{dr}\left(\frac{a_{\mathrm{rad}}}{3}T_\omega^4\right). \tag{36}$$

Here, $\mathcal{F}_{\mathrm{trap}}$ is the baryon number density normalized by the value that can be supported by photon pressure against gravity, $g_{\mathrm{NS}}$ is surface gravitational acceleration of magnetar, and $a_{\mathrm{rad}} = \pi^2/(15c^3)$ [e.g., [85]]. $\mathcal{F}_{\mathrm{trap}} = 1$ corresponds to the case of hydrostatic equilibrium. Based on timescale considerations in Sec. IV A, hydrostatic equilibrium is expected to be established. Nevertheless, we retain $\mathcal{F}_{\mathrm{trap}}$ as a free parameter to allow for the possibility that this assumption can be tested through future x-ray polarization measurements. We set the magnetar mass to be $1.4M_\odot$ and its radius to be 10 km. The electron and positron number densities $n_{\pm,\mathrm{trap}}$ are obtained from the thermal equilibrium condition, as [e.g., [73,86]]

$$n_{\pm,\mathrm{trap}} = \mp\frac{n_{b,\mathrm{trap}}}{2} + \left[\frac{n_{b,\mathrm{trap}}^2}{4} + \left[4\ \max\left(1, \frac{m_e^2c^4b^2}{T_\omega^2}\right)\left(\frac{m_eT_\omega}{2\pi}\right)^3 e^{-2m_ec^2/T_\omega}\right]^{1/2}. \tag{37}$$

For a fireball with a given $\mathcal{F}_{\mathrm{trap}}$, for each photon energy, we obtain the temperature at the photospheric radius using Eq. (35), and then obtain $f$ using Eqs. (2), (36), and (37). Using $\omega$, the magnetic field, and Eqs. (22) and (32), we evaluate $n_{e,\mathrm{res}}$ and $\gamma_{\mathrm{res}}$ for the resonance condition. In the following, $n_{+,\mathrm{trap}} + n_{-,\mathrm{trap}}$ is denoted as $n_{e,\mathrm{trap}}$. The critical photon energy $\omega_{\mathrm{cri}}$ is defined as the energy below which all photons experience vacuum resonance, that is, $n_{e,\mathrm{trap}} > n_{e,\mathrm{res}}$ is satisfied.

The bottom panel of Fig. 3 shows the evaluated pair number density $n_{e,\mathrm{trap}}$ (magenta line) together with the resonance number density $n_{e,\mathrm{res}}$ (black line). The adopted parameters are $B = 10^{13}$ G, $T_b = 10$ keV, $\mathcal{F}_{\mathrm{trap}} = 10$ for fireball, $\theta_{kB} = \pi/4$, $H_{\mathrm{res}} = 10$ cm for propagation. X-mode photons are emitted at $n_{e,\mathrm{trap}}$ and propagate into a lower-density region [84]. The green vertical dashed line marks $\omega_{\mathrm{cri}}$. Sudden decrease of the black line around 100 keV is because of cyclotron resonance, i.e., $u = 1$ [see Eq. (22)]. The modes of propagating photons are also shown by red and blue arrows.

The observed photon spectra in X- and O-mode should be evaluated, taking into account the adiabatic and nonadiabatic mode transformations. For $\omega \geq \omega_{\mathrm{cri}}$ except $\omega \simeq \omega_{B-}$, X-mode photons emitted as $-$ mode ($\omega \gtrsim \omega_{B-}$) or as $+$ mode ($\omega \lesssim \omega_{B-}$) are observed as X-mode. The observed spectra are

$$\frac{dn_{\gamma,\mathrm{X}}}{d\omega}(\omega) = \frac{dn_{\mathrm{BB}}}{d\omega}(T_\omega) \tag{38}$$

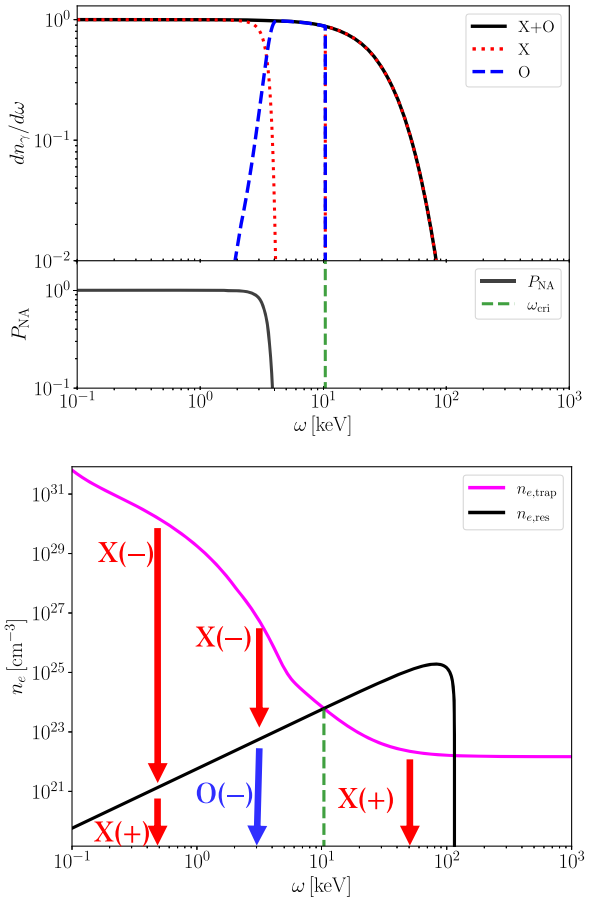



FIG. 3. Observed spectrum from a trapped fireball and pair number densities. Top panel: the black line shows the total observed spectrum, the red dotted line indicates the observed X-mode photons, and the blue dashed line indicates the observed O-mode photons. The lower portion shows the nonadiabatic transition probability. The green vertical line marks $\omega_{\mathrm{cri}}$. Bottom panel: the magenta line shows the number density at which X-mode photons are emitted from the plasma, and the black line shows $n_{e,\mathrm{res}}$ where vacuum resonance occurs. The red and blue arrows indicate the propagation of photons and their typical modes in terms of X/O, rather than $\pm$.

$$\frac{dn_{\gamma,\mathrm{O}}}{d\omega}(\omega) = 0, \tag{39}$$

where $n_{\gamma,\mathrm{I}}$ (I = X/O) is the number density of photon in X/O-mode, and $dn_{\mathrm{BB}}/d\omega(T_\omega)$ is the photon spectrum of the blackbody radiation with temperature $T_\omega$ [84,85]. The possible absorption and scattering are ignored in this work for simplicity. For $\omega < \omega_{\mathrm{cri}}$, X-mode photons are emitted as the $-$ mode (see Fig. 3), and undergo a nonadiabatic transition with probability of $P_{\mathrm{NA}}$ in Eq. (31). Photons that undergo nonadiabatic transitions transform into the $+$ mode and are observed as X-mode, while adiabatically propagating—mode photons are observed as O-mode, due to the MSW-like conversion. Thus, the observed X- and O-mode photons are expressed as

$$\frac{dn_{\gamma,X}}{d\omega}(\omega) = P_{\rm NA}\frac{dn_{\rm BB}}{d\omega}(T_\omega) \tag{40}$$

$$\frac{dn_{\gamma,O}}{d\omega}(\omega) = (1-P_{\rm NA})\frac{dn_{\rm BB}}{d\omega}(T_\omega), \tag{41}$$

where $P_{\rm NA}$ is given by Eq. (31) for each $\omega$.

The top panel of Fig. 3 shows the observed spectrum and polarization. Nonadiabatic transitions efficiently occur in the photon-energy range where both $\omega < \omega_{\rm cri}$ and $P_{\rm NA} \sim 1$ are satisfied. In this energy regime, X-mode photons emitted from the inner region undergo a nonadiabatic transition from their − mode to a + mode, and are therefore observed as X-mode photons (see also Fig. 2 and the bottom panel of Fig. 3). Adiabatic propagation takes place in the photon-energy range where $P_{\rm NA} \sim 0$ is satisfied. In this range, for photons with $\omega < \omega_{\rm cri}$, the emitted X-mode photons propagate adiabatically and, through MSW-like mode conversion, escape as O-mode photons. The adiabatic propagation in this energy range can render the x-ray polarization distinguishable from other energy ranges (top panel of Fig. 3).

Figure 4 shows the $\mathcal{F}_{\rm trap}$ dependences of $\omega_{\rm cri}$ (green lines) and $\omega_{\rm adi}$ (purple lines). The adopted parameters, except $\mathcal{F}_{\rm trap}$ and $B$, are the same as in Fig. 3. The solid, dashed, and dotted lines represent these energies for $B = 10^{13}$ G, $10^{14}$ G, and $10^{15}$ G, respectively. Values of $\mathcal{F}_{\rm trap}$ are taken from $10^{-2}$ to $10^{3}$, with the hydrostatic equilibrium satisfied at $\mathcal{F}_{\rm trap} \sim 1$ [see Eq. (36)]. For a fireball with given $\mathcal{F}_{\rm trap}$, the MSW-like adiabatic mode conversion from X-mode to O-mode occurs in the energy range between the purple and green lines. For the stronger magnetic fields, the energy range of MSW-like conversion becomes narrower due to lower $\omega_{\rm cri}$ and higher $\omega_{\rm adi}$ [Eqs. (11), (12), (33)]. For a fireball with $\mathcal{F}_{\rm trap}$ smaller than the intersection of purple and green lines, MSW-like conversion does not occur, and all photons are emitted in the X-mode. This is equivalent to the bayron-free pair fireball in the limit of $f \to 0$. We note that, in such fireballs, all X-mode photons with $\omega < \omega_{\rm cri}$ undergo nonadiabatic mode transition with probability $P_{\rm NA} \simeq 1$ [see Eq. (34)]. The modification to the polarization becomes more significant for fireballs with more baryons and weaker magnetic fields.

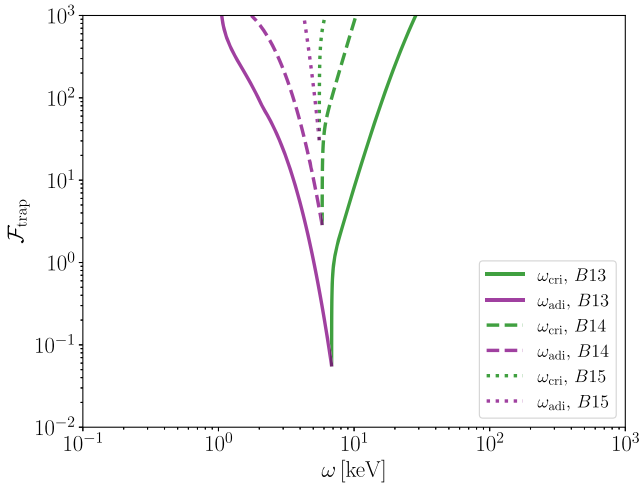



FIG. 4. $\omega_{\rm cri}$ (green line) and $\omega_{\rm adi}$ (purple line) for different baryon loading, $\mathcal{F}_{\rm trap}$. The legends $Bx$ represents the model with $B = 10^x$G.

### C. Polarization of expanding fireballs along open magnetic fields

The dynamics of baryon-loaded expanding fireballs along open magnetic field lines have been modeled in [73]. An expanding fireball is characterized by the surface magnetic field, $B_0$, the initial temperature $T_0$, the initial fireball size $l_0$, and the initial amount of baryon, described by $\mathcal{F}_{\rm exp}$ [87]. A dipole magnetic field is assumed here. The total luminosity of the fireball is given by $\pi l_0^2 c a_{\rm rad} T_0^4$ [67], and the initial rest-mass energy density of baryons is set to be $\mathcal{F}_{\rm exp} a_{\rm rad} T_0^4$.

In this work, we focus on the radiation-dominated fireball. For the fireballs, the radial dependence of comoving temperature, Lorentz factor, and comoving baryon density are [73]

$$T = T_0 \bar{r}^{-3/2}, \tag{42}$$

$$\Gamma = \bar{r}^{3/2}, \tag{43}$$

$$n_{b,\rm exp} = \mathcal{F}_{\rm exp}\frac{a_{\rm rad}T_0^4}{m_b c^2}\bar{r}^{-9/2}, \tag{44}$$

where $\bar{r}$ is the radial coordinate normalized to the magnetar radius. The comoving pair number density is obtained from Eq. (37) with the subscript "trap" replaced by "exp," together with Eqs. (42) and (44). X-mode photons with energy $\omega$ are emitted at the radius where

$$n_{e,\rm exp}\sigma_{\rm T}\min(1,u^{-2})\frac{r}{\Gamma} = 1, \tag{45}$$

is satisfied [88]. For each $\omega$, by solving Eq. (45) for $\bar{r}$, and using Eq. (42), we obtain the plasma temperature $T_\omega$ at the photospheric radius. The emitted photon spectrum at $\omega$ is obtained from a blackbody radiation with temperature $T_\omega$. Using Eqs. (38)–(41), we evaluate the observed spectrum and polarization for the expanding fireball.

Figure 5 shows the observed spectrum and polarization. The adopted parameters are $B_0 = 2\times10^{14}$ G, $T_0 = 80$ keV, $l_0 = 5\times10^3$ cm, $\mathcal{F}_{\rm exp} = 10^{-2}$ for the fireball based on [73], and $H_{\rm res} = 10^6$ cm, $\theta_{kB} = 0.1$, for the propagation. As in the trapped-fireball case, photons with $\omega_{\rm ad} \lesssim \omega < \omega_{\rm cri}$ undergo an MSW-like mode conversion, in which the emitted X-mode photons are converted into observed

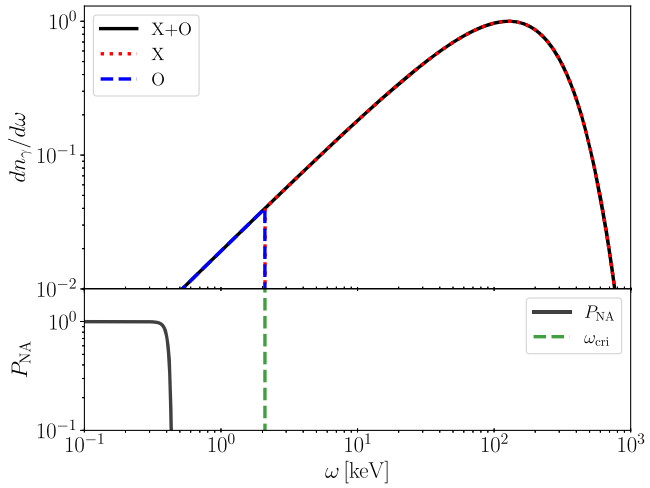



FIG. 5. Observed spectrum from an expanding fireball. Each line has the same meaning as the top panel of Fig. 3.

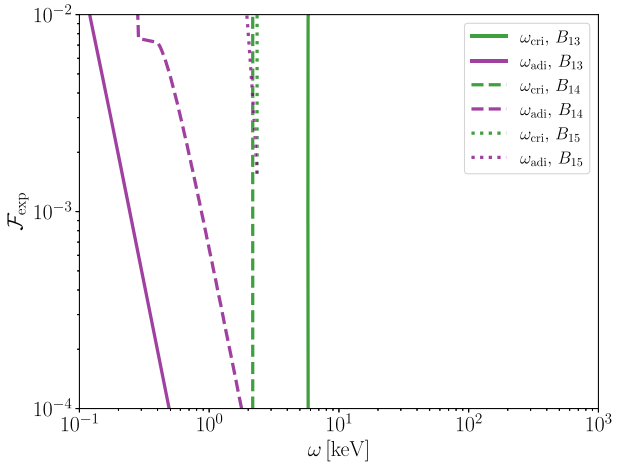



FIG. 6. $\omega_{\rm cri}$ (green line) and $\omega_{\rm adi}$ (purple line) for different baryon loading, $\mathcal{F}_{\rm exp}$. Each line has the same meaning as Fig. 4.

O-mode photons while remaining in the eigenmode of the propagation, − mode (see Fig. 2).

Figure 6 shows $\mathcal{F}_{\rm exp}$-dependences of $\omega_{\rm cri}$ (green line) and $\omega_{\rm adi}$ (purple line). Adopted parameters except $\mathcal{F}_{\rm exp}$ are the same as Fig. 5. $\mathcal{F}_{\rm exp}$ are chosen from $10^{-4}$ to $10^{-2}$, above which the approximation of radiation-dominant fireball is broken ([73] for details). The bending around $\mathcal{F}_{\rm exp} \sim 8 \times 10^{-3}$ in the case of $B = 10^{14}$ G arises because the ion cyclotron resonance, proportional to $(1-u_b)^2$, affects the determination of $\omega_{\rm adi}$ in solving Eq. (33). For $B = 10^{15}$ G, $\omega_{\rm adi}$ shows little dependence on $\mathcal{F}_{\rm exp}$ because photons escape from the hot inner region dominated by pair plasma, due to the strong suppression on the cross section [see Eq. (45)]. For the cases of $B = 10^{13}$ G and $10^{14}$ G, the MSW-like conversion into O-mode occurs in relatively large parameter ranges compared to the trapped fireball, and these ranges depend on $\mathcal{F}_{\rm exp}$. This suggests the possibility of measuring baryon-loading using x-ray polarization for given $B_0$.

## V. SUMMARY AND DISCUSSION

We have developed a framework to describe vacuum resonance in the three-component plasma produced in baryon-loaded magnetar bursts, and revealed the polarization of x-ray bursts expected in future observations. By parametrizing the plasma composition, we derived the normal modes, their polarization properties, and their dependence on composition (Sec. II). We showed that the vacuum resonance, previously studied in the context of magnetar persistent surface emission [26], can also occur in magnetar bursts. The resonance condition, given in Eq. (22), depends only on the pair number density $n_e$. We also investigate the MSW-like mode conversion and the nonadiabatic transitions of normal modes at the resonance, whose probability, especially $f$-dependence, is given in Eqs. (31) and (32) (Sec. III). Applying the framework to analytic fireball models, we demonstrated that vacuum resonance appears in the observed x-ray polarization (Sec. IV). Throughout these works, we also clarified the connection between the polarization modes in conventional purely pair fireballs and those in baryon-loaded fireballs. The nonadiabatic mode transition plays an important role in the X/O-mode propagation in a pair plasma, as shown in Eq. (34). Our results suggest that polarization observations of magnetar bursts can provide unique diagnostics of the fireball structures and their composition.

In the modeling presented in Sec. IV, the observerd spectrum has been calculated using simplified models, with fixed parameters, $B$, $\theta_{kB}$, $\mathcal{F}_{\rm trap/\,exp}$, and $H_{\rm res}$. Moreover, the time variability of the amount of baryon is ignored. In reality, the spectrum should be a superposition of emissions with different parameter values and depend on time. A realistic calculation therefore requires time-dependent three-dimensional simulations that incorporate the full structure of fireball [74]. The spectra in this work can serve as initial conditions for such global simulations. The observed spectrum is also expected to be modified by the absorption and scattering of O-mode photons, as well as by resonant Compton scattering in the magnetosphere [44,73,89]. For magnetar persistent surface emission, rather than bursts, the presence of a hot coronal region composed of pair plasmas near the surface might necessitate considering a three-component plasma, studied in this work. These realistic global calculations are left for future study.

The polarization signature depends on the baryon content of fireballs (Sec. IV), so observations of x-ray polarization may serve as a probe of the baryon loading in fireballs. [73] investigated the relation between FRB 20200428A and simultaneously observed SB within the expanding-fireball model. They showed that mildly

baryon-loaded fireballs produce higher kinetic energy in the plasma outflow, which may lead to FRB emission. On the other hand, [90] proposed that x-ray polarization of SBs can be useful to distinguish between expanding and trapped fireball configurations. The polarization induced by the vacuum resonance studied in this paper may provide a means to constrain the amount of baryon lading on fireballs (see Fig. 6) by the observation of x-ray polarization. By combining this work and [90], future simultaneous observation of FRBs and SB polarizations would enable the determination of the fireball configuration as well as its baryon loading, providing a powerful probe of the still-unclear FRB emission mechanism.

## ACKNOWLEDGMENTS

We thank K. Asano, T. Kawashima, and J. Shimoda for comments leading this research area and occasional discussions. We also thank the anonymous referee for many valuable comments that helped improve the manuscript. This work is supported by JSPS KAKENHI Grant-in-Aid for Scientific Research No. JP25KJ0024 and No. JP25K17378.

## DATA AVAILABILITY

The data that support the findings of this article are not publicly available. The data are available from the authors upon reasonable request.

[1] R. C. Duncan and C. Thompson, Formation of very strongly magnetized neutron stars: Implications for gamma-ray bursts, Astrophys. J. Lett. **392**, L9 (1992).
[2] J. S. Heyl and L. Hernquist, A QED model for the origin of bursts from soft gamma repeaters and anomalous X-ray pulsars, Astrophys. J. **618**, 463 (2005).
[3] A. K. Harding and D. Lai, Physics of strongly magnetized neutron stars, Rep. Prog. Phys. **69**, 2631 (2006).
[4] V. M. Kaspi and A. M. Beloborodov, Magnetars, Annu. Rev. **55**, 261 (2017).
[5] T. Enoto, S. Kisaka, and S. Shibata, Observational diversity of magnetized neutron stars, Rep. Prog. Phys. **82**, 106901 (2019).
[6] C. Thompson and R. C. Duncan, The soft gamma repeaters as very strongly magnetized neutron stars—I. Radiative mechanism for outbursts, Mon. Not. R. Astron. Soc. **275**, 255 (1995).
[7] C. Thompson and R. C. Duncan, The soft gamma repeaters as very strongly magnetized neutron stars. II. Quiescent neutrino, X-ray, and alfven wave emission, Astrophys. J. **473**, 322 (1996).
[8] T. Wada, K. Ioka, and B. Zhang, Binary comb models for FRB 121102, Astrophys. J. **920**, 54 (2021).
[9] T. Wada and J. Shimoda, The Dzhanibekov effect as a possible source of magnetar activity, Astrophys. J. **972**, 58 (2024).
[10] J. Shimoda and T. Wada, On acceleration of highest-energy cosmic rays in a novel scenario of magnetar transients, Astrophys. J. **986**, 213 (2025).
[11] T. Wada and S. S. Kimura, Spectral shapes of pair annihilation line emission in magnetar giant flares (to be published).
[12] P. Meszaros, *High-Energy Radiation from Magnetized Neutron Stars* (University of Chicago Press, Chicago, 1992).
[13] J. S. Heyl and L. Hernquist, Analytic form for the effective Lagrangian of QED and its application to pair production and photon splitting, Phys. Rev. D **55**, 2449 (1997).
[14] W.-Y. Tsai and T. Erber, Propagation of photons in homogeneous magnetic fields: Index of refraction, Phys. Rev. D **12**, 1132 (1975).
[15] W. Heisenberg and H. Euler, Folgerungen aus der Diracschen Theorie des Positrons, Z. Phys. **98**, 714 (1936).
[16] J. Schwinger, On gauge invariance and vacuum polarization, Phys. Rev. **82**, 664 (1951).
[17] Y. N. Gnedin and G. G. Pavlov, The transfer equations for normal waves and radiation polarization in an anisotropic medium, Sov. J. Exp. Theor. Phys. **38**, 903 (1974).
[18] P. Meszaros and J. Ventura, Vacuum polarization effects on radiative opacities in a strong magnetic field, Phys. Rev. D **19**, 3565 (1979).
[19] W. C. G. Ho and D. Lai, Atmospheres and spectra of strongly magnetized neutron stars, Mon. Not. R. Astron. Soc. **327**, 1081 (2001).
[20] Y. N. Gnedin, G. G. Pavlov, and Y. A. Shibanov, The effect of vacuum birefringence in a magnetic field on the polarization and beaming of X-ray pulsars, Sov. Astron. Lett. **4**, 117 (1978).
[21] G. G. Pavlov and Y. A. Shibanov, Influence of vacuum polarization by a magnetic field on the propagation of electromagnetic waves in a plasma, Sov. J. Exp. Theor. Phys. **49**, 741 (1979).
[22] M. Soffel, J. Ventura, H. Herold, H. Ruder, and W. Nagel, Propagation of high frequency waves in strongly magnetized plasmas—mode ambiguities due to vacuum polarization, Astron. Astrophys. **126**, 251 (1983).
[23] D. Lai and W. C. G. Ho, Resonant conversion of photon modes due to vacuum polarization in a magnetized plasma: Implications for X-ray emission from magnetars, Astrophys. J. **566**, 373 (2002).
[24] P. Goldreich and W. H. Julian, Pulsar electrodynamics, Astrophys. J. **157**, 869 (1969).
[25] D. Lai and W. C. G. Ho, Transfer of polarized radiation in strongly magnetized plasmas and thermal emission from magnetars: Effect of vacuum polarization, Astrophys. J. **588**, 962 (2003).

[26] D. Lai and W. C. Ho, Polarized X-ray emission from magnetized neutron stars: Signature of strong-field vacuum polarization, Phys. Rev. Lett. **91**, 071101 (2003).
[27] W. C. G. Ho and D. Lai, Atmospheres and spectra of strongly magnetized neutron stars—II. The effect of vacuum polarization, Mon. Not. R. Astron. Soc. **338**, 233 (2003).
[28] W. C. G. Ho, D. Lai, A. Y. Potekhin, and G. Chabrier, Atmospheres and spectra of strongly magnetized neutron stars. III. Partially ionized hydrogen models, Astrophys. J. **599**, 1293 (2003).
[29] F. Özel, The effect of vacuum polarization and proton cyclotron resonances on photon propagation in strongly magnetized plasmas, Astrophys. J. **583**, 402 (2003).
[30] W. C. G. Ho and D. Lai, Spectral features in the thermal emission from isolated neutron stars: Dependence on magnetic field strengths, Astrophys. J. **607**, 420 (2004).
[31] J. Niemiec and T. Bulik, Radiation spectra and polarization in magnetar bursts, Astrophys. J. **637**, 466 (2006).
[32] M. van Adelsberg and D. Lai, Atmosphere models of magnetized neutron stars: QED effects, radiation spectra and polarization signals, Mon. Not. R. Astron. Soc. **373**, 1495 (2006).
[33] R. Fernández and S. W. Davis, The X-ray polarization signature of quiescent magnetars: Effect of magnetospheric scattering and vacuum polarization, Astrophys. J. **730**, 131 (2011).
[34] R. M. E. Kelly, S. Zane, R. Turolla, and R. Taverna, X-ray polarization in magnetar atmospheres—effects of mode conversion, Mon. Not. R. Astron. Soc. **528**, 3927 (2024).
[35] C. Wang and D. Lai, Wave modes in the magnetospheres of pulsars and magnetars, Mon. Not. R. Astron. Soc. **377**, 1095 (2007).
[36] M. C. Weisskopf *et al.*, The imaging X-ray polarimetry explorer (IXPE): Pre-launch, J. Astron. Telesc. Instrum. Syst. **8**, 026002 (2022).
[37] R. Taverna *et al.*, Polarized x-rays from a magnetar, Science **378**, 646 (2022).
[38] S. Zane *et al.*, A strong X-ray polarization signal from the magnetar 1RXS J170849.0-400910, Astrophys. J. Lett. **944**, L27 (2023).
[39] J. Heyl *et al.*, The detection of polarized X-ray emission from the magnetar 1E 2259 + 586, Mon. Not. R. Astron. Soc. **527**, 12219 (2024).
[40] R. Turolla *et al.*, IXPE and XMM-Newton observations of the soft gamma repeater SGR 1806-20, Astrophys. J. **954**, 88 (2023).
[41] M. Rigoselli *et al.*, IXPE detection of highly polarized X-rays from the magnetar 1E 1841-045, Astrophys. J. Lett. **985**, L34 (2025).
[42] R. Stewart *et al.*, X-ray polarization of the magnetar 1E 1841-045, Astrophys. J. Lett. **985**, L35 (2025).
[43] D. Lai, IXPE detection of polarized X-rays from magnetars and photon mode conversion at QED vacuum resonance, Proc. Natl. Acad. Sci. U.S.A. **120**, e2216534120 (2023).
[44] C. Thompson, M. Lyutikov, and S. R. Kulkarni, Electrodynamics of magnetars: Implications for the persistent X-ray emission and spin-down of the soft gamma repeaters and anomalous X-ray pulsars, Astrophys. J. **574**, 332 (2002).
[45] R. Taverna, R. Turolla, V. Suleimanov, A. Y. Potekhin, and S. Zane, X-ray spectra and polarization from magnetar candidates, Mon. Not. R. Astron. Soc. **492**, 5057 (2020).
[46] M. Ge *et al.*, Physics of strong magnetism with eXTP, Sci. China Phys. Mech. Astron. **68**, 119505 (2025).
[47] I. Demidov and Y. Lyubarsky, Radiatively driven evaporation from magnetar's surface, Mon. Not. R. Astron. Soc. **518**, 810 (2023).
[48] J. Goodman, Are gamma-ray bursts optically thick?, Astrophys. J. Lett. **308**, L47 (1986).
[49] B. Paczynski, Gamma-ray bursters at cosmological distances, Astrophys. J. Lett. **308**, L43 (1986).
[50] A. Shemi and T. Piran, The appearance of cosmic fireballs, Astrophys. J. Lett. **365**, L55 (1990).
[51] P. Meszaros, P. Laguna, and M. J. Rees, Gasdynamics of relativistically expanding gamma-ray burst sources: Kinematics, energetics, magnetic fields, and efficiency, Astrophys. J. **415**, 181 (1993).
[52] P. Mészáros and M. J. Rees, Steep slopes and preferred breaks in gamma-ray burst spectra: The role of photospheres and comptonization, Astrophys. J. **530**, 292 (2000).
[53] K. Hurley *et al.*, An exceptionally bright flare from SGR 1806-20 and the origins of short-duration $\gamma$-ray bursts, Nature (London) **434**, 1098 (2005).
[54] S. Mereghetti, D. Götz, A. von Kienlin, A. Rau, G. Lichti, G. Weidenspointner, and P. Jean, The first giant flare from SGR 1806-20: Observations using the anticoincidence shield of the spectrometer on INTEGRAL, Astrophys. J. Lett. **624**, L105 (2005).
[55] S. E. Boggs, A. Zoglauer, E. Bellm, K. Hurley, R. P. Lin, D. M. Smith, C. Wigger, and W. Hajdas, The giant flare of 2004 december 27 from SGR 1806-20, Astrophys. J. **661**, 458 (2007).
[56] D. D. Frederiks, S. V. Golenetskii, V. D. Palshin, R. L. Aptekar, V. N. Ilyinskii, F. P. Oleinik, E. P. Mazets, and T. L. Cline, Giant flare in SGR 1806-20 and its Compton reflection from the moon, Astron. Lett. **33**, 1 (2007).
[57] B. M. Gaensler *et al.*, An expanding radio nebula produced by a giant flare from the magnetar SGR 1806-20, Nature (London) **434**, 1104 (2005).
[58] P. B. Cameron *et al.*, Detection of a radio counterpart to the 27 december 2004 giant flare from SGR 1806–20, Nature (London) **434**, 1112 (2005).
[59] E. Nakar, T. Piran, and R. Sari, Pure and loaded fireballs in soft gamma-ray repeater giant flares, Astrophys. J. **635**, 516 (2005).
[60] C. Thompson and R. C. Duncan, The giant flare of 1998 august 27 from SGR 1900 + 14. II. Radiative mechanism and physical constraints on the source, Astrophys. J. **561**, 980 (2001).
[61] C. D. Bochenek, V. Ravi, K. V. Belov, G. Hallinan, J. Kocz, S. R. Kulkarni, and D. L. McKenna, A fast radio burst associated with a galactic magnetar, Nature (London) **587**, 59 (2020).
[62] B. C. Andersen *et al.* (CHIME/FRB Collaboration), A bright millisecond-duration radio burst from a galactic magnetar, Nature (London) **587**, 54 (2020).
[63] S. Mereghetti *et al.*, INTEGRAL discovery of a burst with associated radio emission from the magnetar SGR 1935 + 2154, Astrophys. J. Lett. **898**, L29 (2020).

[64] C. K. Li *et al.*, HXMT identification of a non-thermal X-ray burst from SGR J1935 + 2154 and with FRB 200428, Nat. Astron. **5**, 378 (2021).
[65] A. Ridnaia, D. Svinkin, D. Frederiks, A. Bykov, S. Popov, R. Aptekar, S. Golenetskii, A. Lysenko, A. Tsvetkova, M. Ulanov, and T. L. Cline, A peculiar hard X-ray counterpart of a galactic fast radio burst, Nat. Astron. **5**, 372 (2021).
[66] M. Tavani *et al.*, An X-ray burst from a magnetar enlightening the mechanism of fast radio bursts, Nat. Astron. **5**, 401 (2021).
[67] K. Ioka, Fast radio burst breakouts from magnetar burst fireballs, Astrophys. J. Lett. **904**, L15 (2020).
[68] Y.-P. Yang and B. Zhang, Fast radio bursts and their High-energy counterparts from magnetar magnetospheres, Astrophys. J. **919**, 89 (2021).
[69] T. Wada and K. Asano, Radiative acceleration and X-ray spectrum of an outflowing pure electron-positron pair fireball in magnetar bursts, Prog. Theor. Exp. Phys. **2025**, 033E01 (2025).
[70] W. Lu, P. Kumar, and B. Zhang, A unified picture of galactic and cosmological fast radio bursts, Mon. Not. R. Astron. Soc. **498**, 1397 (2020).
[71] J. I. Katz, The FRB-SGR connection, Mon. Not. R. Astron. Soc. **499**, 2319 (2020).
[72] S. Yamasaki, K. Kashiyama, and K. Murase, Multi-wavelength constraints on the outflow properties of the extremely bright millisecond radio bursts from the galactic magnetar SGR 1935 + 2154, Mon. Not. R. Astron. Soc. **511**, 3138 (2022).
[73] T. Wada and K. Ioka, Expanding fireball in magnetar bursts and fast radio bursts, Mon. Not. R. Astron. Soc. **519**, 4094 (2023).
[74] Y.-P. Yang and B. Zhang, On the polarization properties of magnetar giant flare pulsating tails, Astrophys. J. **815**, 45 (2015).
[75] The sign of $g_V\eta_V \cos\theta_{kB}/(\epsilon_V \sin^2\theta_{kB} + \eta_V \cos\theta_{kB})$ in front of the square root is incorporated into the definition of $K_\pm$.
[76] V. Canuto, J. Lodenquai, and M. Ruderman, Thomson scattering in a strong magnetic field, Phys. Rev. D **3**, 2303 (1971).
[77] H. Herold, Compton and Thomson scattering in strong magnetic fields, Phys. Rev. D **19**, 2868 (1979).
[78] L. D. Landau, To the theory of energy transmission in collissions. II, Phys. Zs. Sowjet **2**, 46 (1932).
[79] C. Zener, Non-adiabatic crossing of energy levels, Proc. R. Soc. A **137**, 696 (1932).
[80] S. J. Parke, Nonadiabatic level crossing in resonant neutrino oscillations, Phys. Rev. Lett. **57**, 1275 (1986).
[81] W. C. Haxton, The solar neutrino problem, Annu. Rev. **33**, 459 (1995).
[82] The definition of $\omega_{\rm adi}$ is modified from that in [23] by a factor of $(2/\pi)^{1/3}$, so that $\omega = \omega_{\rm adi}$ corresponds to $P_{\rm NA} = \exp(-1)$. Exactly, Eq. (33) should be solved for $\omega$ appearing in $u_b$.
[83] N. Chamel and P. Haensel, Physics of neutron star crusts, Living Rev. Relativity **11**, 10 (2008).
[84] Y. E. Lyubarsky, On the X-ray spectra of soft gamma repeaters, Mon. Not. R. Astron. Soc. **332**, 199 (2002).
[85] G. B. Rybicki and A. P. Lightman, *Radiative Processes in Astrophysics* (John Wiley & Sons, New York, 1979).
[86] L. D. Landau and E. M. Lifshitz, *Statistical Physics Part I*, 3rd ed. (Elsevier, Amsterdam, 1980).sp80.
[87] $\mathcal{F}_{\rm exp}$ corresponds to $\eta^{-1}$ in [73].
[88] M. A. Abramowicz, I. D. Novikov, and B. Paczynski, The appearance of highly relativistic, spherically symmetric stellar winds, Astrophys. J. **369**, 175 (1991).
[89] S. Yamasaki, Y. Lyubarsky, J. Granot, and E. Göğüş, Spectral modification of magnetar flares by resonant cyclotron scattering, Mon. Not. R. Astron. Soc. **498**, 484 (2020).
[90] S.-Q. Zhong, L. Li, B. Zhang, and Z.-G. Dai, Identifying the origin of fast radio burst–associated X-ray bursts with X-ray polarization, Astrophys. J. **976**, 52 (2024).